Supplement of The Cryosphere, 20, 573–593, 2026
https://doi.org/10.5194/tc-20-573-2026-supplement

The Cryosphere Open Access EGU

Supplement of

On the accuracy of the measured and modelled surface latent and sensible heat flux in the interior of the Greenland Ice Sheet

Ida Haven et al.

Correspondence to: Ida Haven (idahaven@kpnmail.nl) and Hans Christian Steen-Larsen (Hans.Christian.Steen-Larsen@uib.no)

Supplementary Materials

S1 Footprint

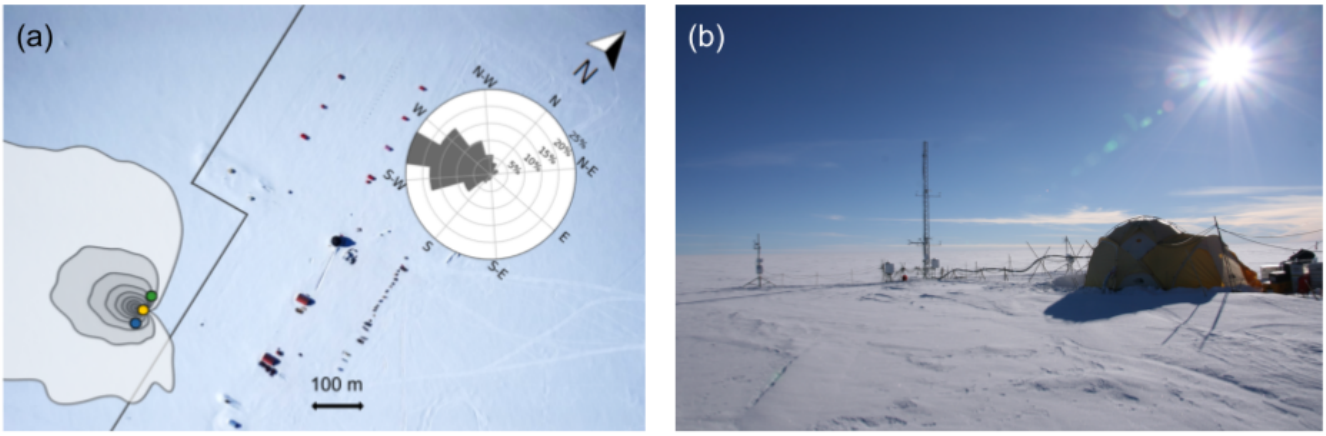

Figure S1. (a) Camp overview, similar to figure 1b, with contours indicating the EC-IRGASON flux footprint, computed following Kljun et al. (2015) using a boundary layer height of 200 m (Rozmiarek et al., 2025). The contours and shading indicate the percentage of source area in steps of 10 %, going from 10 % to 80 %. (b) A view of the footprint and the landscape in the windward direction.

S2 Emissivity sensitivity

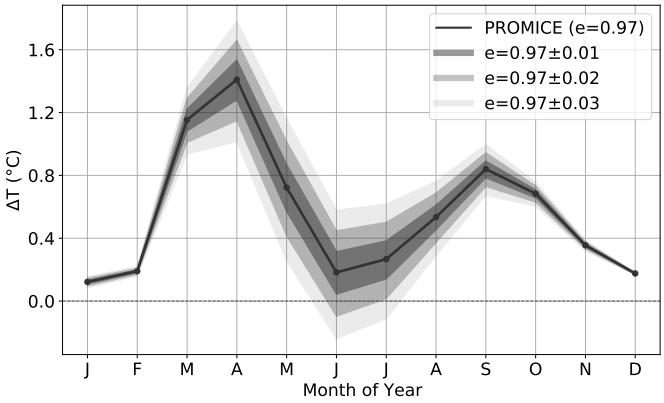

Figure S2. Seasonal cycle of the PROMICE near-surface atmospheric temperature gradient (2 m - surface temperature), with the shaded areas showing the temperature gradient when the surface temperature is computed using different emissivities.

S3 Spectra comparison

To check the validity of using the Kaimal et al. (1972) spectrum for the Moore (1986) correction, the 30-minute (co)spectra of w, T, a, $w'T'$ and $w'a'$ are computed, where a is the absolute humidity. The cospectrum $S_{w\chi}(f)$ of time series w' and χ' is

defined, like in Van Tiggelen (2023), as the real part of the cross-spectrum with frequency f and describes how the turbulent flux information is distributed in the frequency space:

$$S_{wX}(f) = \mathcal{R}\left[\mathcal{F}_w(f) \cdot \mathcal{F}_\chi^*(f)\right] \tag{S1}$$

Where $\mathcal{F}_\chi^*(f)$ is the complex conjugate of $\mathcal{F}_\chi(f)$, which is the Fourier transform of the signal $\chi'(t)$ and is defined as:

$$\mathcal{F}_\chi(f) = \frac{1}{\sqrt{2}} \int_{-\infty}^{+\infty} \chi'(t) e^{ift} \mathrm{dt}. \tag{S2}$$

Since the spectra are quite sensitive to noise, the period of the 1st to the 6th of June is chosen, which is a period with calm and clearsky conditions. The cospectra are computed using the TK3 working memory, which provides the raw data on which the unit conversion, despiking and cross-correlation correction are already applied. Planar fit correction is applied manually using the planar fit coefficients provided by TK3. The S_{ww}, S_{aa}, S_{TT}, S_{wT}, S_{wa} cospectra and frequencies are then normalized in the following way:

$$\text{Normalized spectrum} = \frac{f S_{xx}(f)}{\overline{x'x'}} \tag{S3a}$$

$$\text{Normalized frequency: } n = \frac{fz}{U} \tag{S3b}$$

In general, only the spectra are used for the intervals that have passed the post-processing criteria (described in Sect 3.1). However, an extra round of filtering is applied to get the cleanest spectra. So the following criteria are added:

- $3\,\mathrm{m\,s^{-1}} < U < 8\,\mathrm{m\,s^{-1}}$
- $\left| \frac{\overline{v'w'}}{\overline{u'w'}} \right| < 0.25$

Where the first point strengthens the windspeed criteria to assure turbulent exchange and the second is a good quality parameter. Two intervals which passed these criteria, but still showed a high amount of noise were manually removed, leaving a total of 109 spectra. Two rounds of averaging are applied over the resulting spectra, first averaging all the spectra based on frequency and then averaging this result over bins ranging from n = 0.01 to n = 6. The S_{ww}, S_{wT} and S_{wa} spectra are also compared to the Kaimal et al. (1972) spectrum. For this, the equations used in TK3 are applied (Mauder and Foken, 2015), which are based on Moore (1986) and Kaimal et al. (1972).

For stable conditions (z/L $<$ 0): For $\overline{w'w'}$:

$$\frac{f \cdot S_{ww}(f)}{\overline{w'w'}} = \frac{n}{A_w + 3.124 \cdot (A_w)^{-2/3} \cdot n^{5/3}} \tag{S4a}$$

$$A_w = 0.838 + 1.172 \cdot \frac{z}{L} \tag{S4b}$$

For $\overline{w'T'}$ and $\overline{w'a'}$:

$$\frac{f \cdot S_{xy}(f)}{u_* \cdot y_*} = \frac{0.88 \frac{n}{n_0}}{1 + 1.5 \cdot \left(\frac{n}{n_0}\right)^{2.1}} \tag{S5a}$$

$$n_{0,wT} = 0.23 \cdot \left(1 + 6.4 \frac{z}{L}\right)^{0.75} \tag{S5b}$$

Unstable conditions (z/L $\geq$ 0): For $\overline{w'w'}$:

$$\frac{f \cdot S_w w(f)}{u_*^2} = \frac{2n}{1 + 5.3n^{5/3}} + \frac{32n\zeta}{(1 + 17n)^{5/3}} \tag{S6a}$$

$$\zeta = \left(\frac{z}{-L} \right)^{2/3} \tag{S6b}$$

For $\overline{w'T'}$ and $\overline{w'a'}$:

$$\frac{f \cdot S_{wT}(f)}{\overline{w'T'}} = \begin{cases} \frac{11n}{(1+13.3n)^{1.75}} & n < 1 \\ \frac{4.4n}{(1+3.8n)^{2.4}} & n \geq 1 \end{cases} \tag{S7}$$

The resulting spectra are provided in Figure S3.

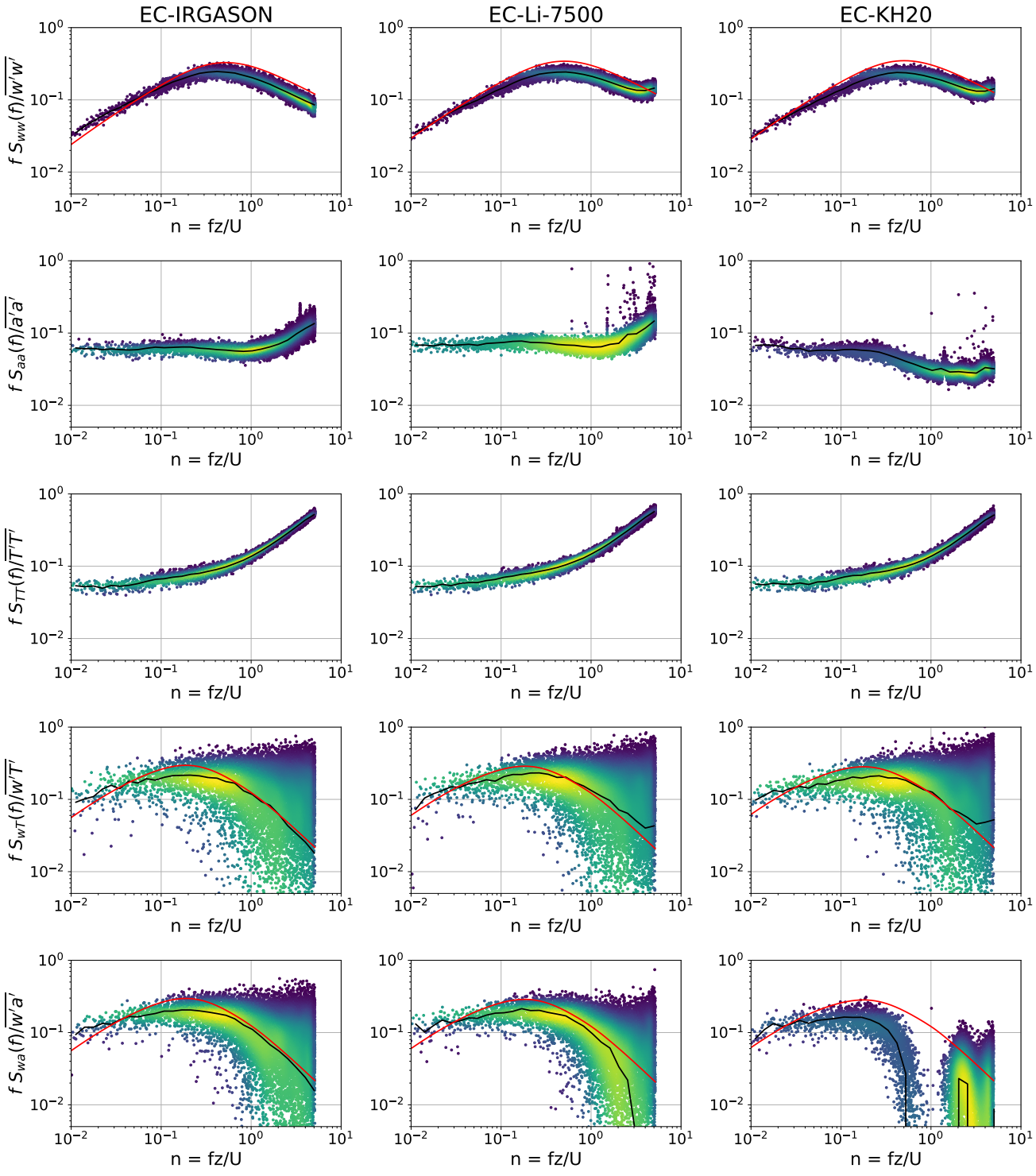

Figure S3. Normalised S_{ww}, S_{TT}, S_{aa}, S_{wT} and S_{wa} spectrum of the EC-IRGASON, EC-Li-7500 and EC-KH20. The dots show the frequency-averaged spectrum, where the colour scale indicates the density of the scatter and increasing brightness corresponds to increasing scatter density. The black line shows the frequency- and bin-averaged spectrum and the red line is the Kaimal spectrum.

S4 Data filtering

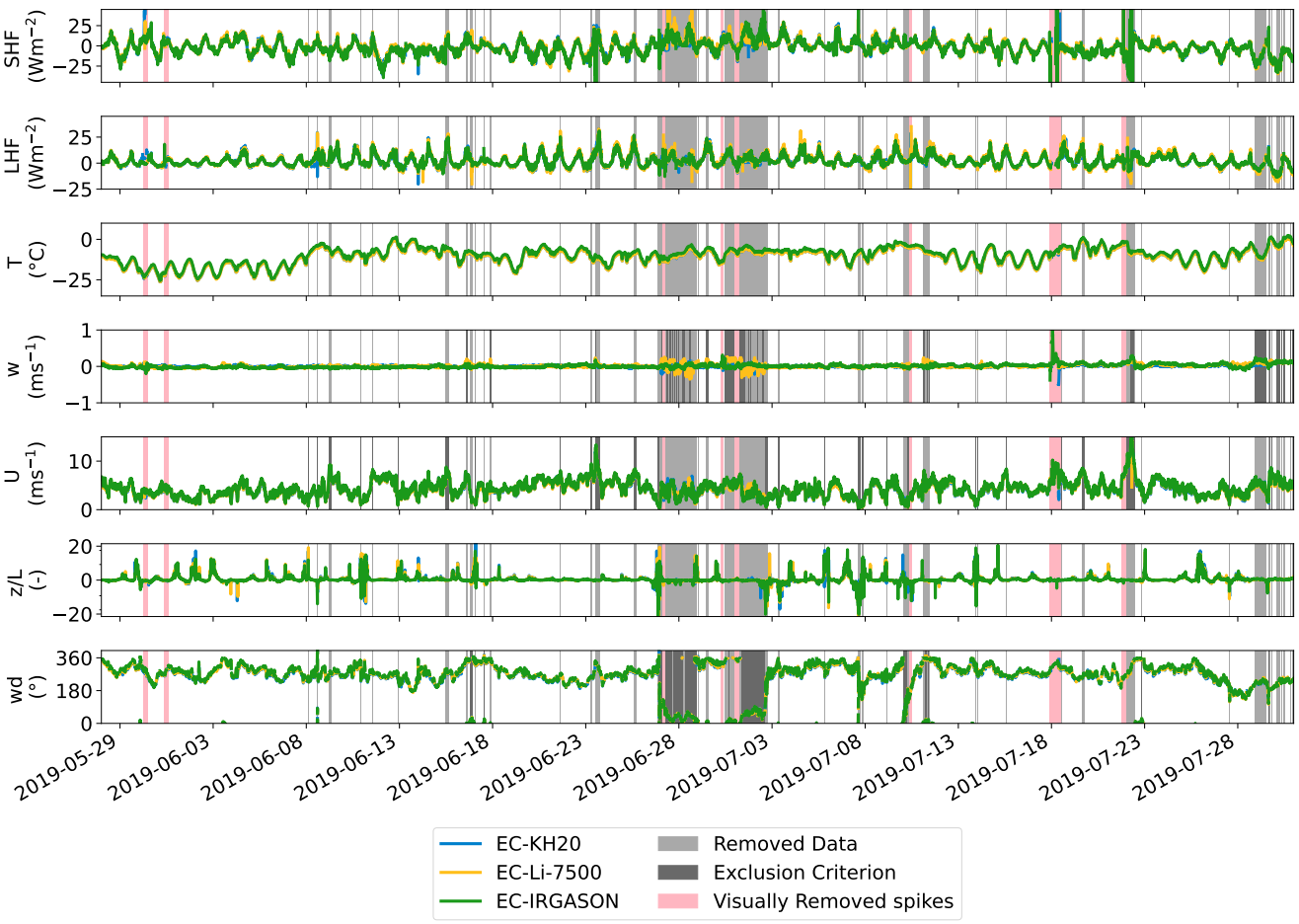

Figure S4. Timeseries of 10-minute averaged EC data after TK3 processing, but before post-processing filtering. In grey, the data removed based on the filtering criteria is shown, where dark grey indicates the variable(s) that did not meet the conditions. In pink, the data that is removed based on the visual inspection is indicated. The stability (z/L) is plotted on a symmetrical log scale, where the part between -1 and 1 is linear and values outside are plotted on a log scale.

S5 Separated slopes

Table S1. Slopes from the data displayed in Fig.5abc, for only positive and negative LHF measured by the EC-IRGASON

Bulk LHF	LHF EC-IRGASON >0	LHF EC-IRGASON <0
PROMICE orig $z_{0,m}$ = $1\mathrm{e}-3\,\mathrm{m}$, $z_{0,q}$ = Smeets and Van den Broeke (2008a, b)	2.09	2.27
PROMICE calc $z_{0,m}$ = $1.3\mathrm{e}-4\,\mathrm{m}$, $z_{0,q}$ = Andreas (1987)	1.36	1.49
PROMICE calc $z_{0,m}$ = $1.3\mathrm{e}-4\,\mathrm{m}$, $z_{0,q}$ = $5.7\mathrm{e}-7\,\mathrm{m}$	0.9	0.98

Table S2. Slopes from the data displayed in Fig.5efg, for only positive and negative SHF measured by the EC-IRGASON

Bulk SHF	SHF EC-IRGASON >0	SHF EC-IRGASON <0
PROMICE orig $z_{0,m}$ = $1\mathrm{e}-3\,\mathrm{m}$, $z_{0,q}$ = Smeets and Van den Broeke (2008a, b)	1.23	1.29
PROMICE calc $z_{0,m}$ = $1.3\mathrm{e}-4\,\mathrm{m}$, $z_{0,q}$ = Andreas (1987)	0.78	0.84
PROMICE calc $z_{0,m}$ = $1.3\mathrm{e}-4\,\mathrm{m}$, $z_{0,q}$ = $2.9\mathrm{e}-4\,\mathrm{m}$	0.87	0.94

S6 Roughness length optimization

Two approaches were used to find an optimised roughness length suitable for bulk calculating both the LHF and SHF. The first approach is using the Andreas (1987) parameterisation to obtain $z_{0,t}$ and assuming $z_{0,q}$ = $z_{0,t}$. The second is using the Andreas (1987) parameterisation for both $z_{0,t}$ and $z_{0,q}$. For a discrete number of $z_{0,u}$ ($1\mathrm{e}-9\,\mathrm{m}$, $1\mathrm{e}-8\,\mathrm{m}$, $1\mathrm{e}-7\,\mathrm{m}$, $1\mathrm{e}-6\,\mathrm{m}$, $5\mathrm{e}-6\,\mathrm{m}$, $1\mathrm{e}-5\,\mathrm{m}$, $5\mathrm{e}-5\,\mathrm{m}$, $1\mathrm{e}-4\,\mathrm{m}$, $1\mathrm{e}-3\,\mathrm{m}$), the slopes of the correlation between the computed bulk and measured EC flux (similar to figure 5) were computed, where a slope close to 1 indicates a correctly simulated diurnal flux amplitude. In figure S5 the slopes of the correlation between the bulk method and the EC are shown for the range of $z_{0,u}$ values. The figure shows that there is no optimised $z_{0,u}$ value using the Andreas parameterisation for both approaches that is suitable for both the LHF and the SHF.

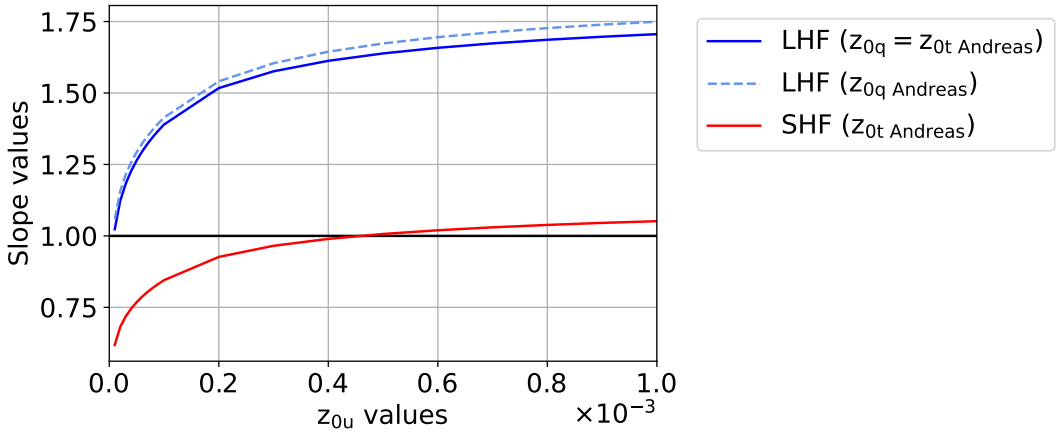

Figure S5. Slopes of the correlation between the computed bulk and measured EC LHF and SHF for a range of $z_{0,u}$ values, using either the Andreas (1987) parameterisation for obtaining both $z_{0,q}$ and $z_{0,t}$ or using the Andreas (1987) parameterisation for obtaining $z_{0,t}$ and assuming that $z_{0,q} = z_{0,t}$.

S7 Roughness length sensitivity

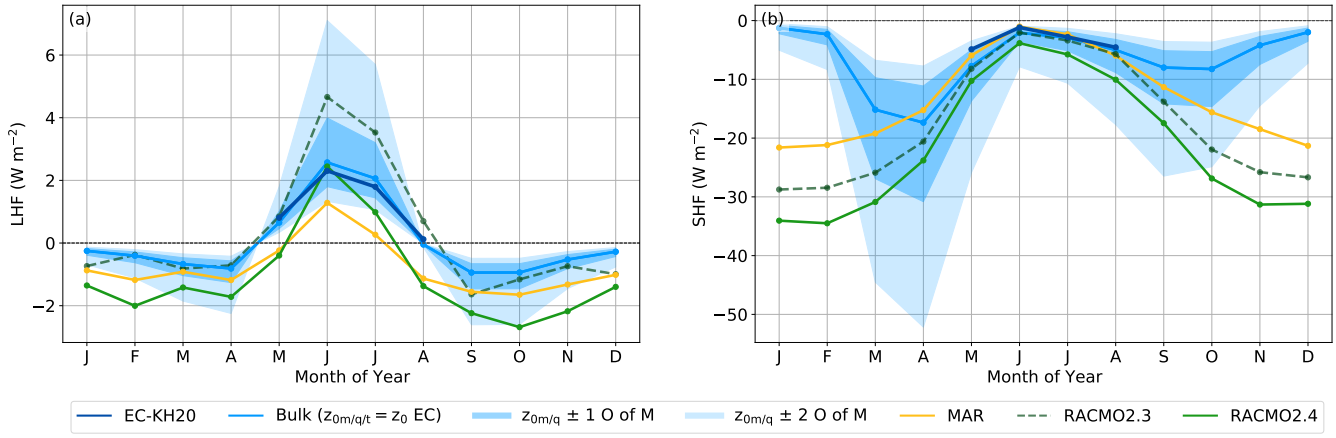

Figure S6. Seasonal cycle of the (a) LHF and (b) SHF from figures 6a and 7a, respectively, with the shaded areas indicating the LHF and SHF calculated from the PROMICE AWS data, using values for $z_{0,u}$, $z_{0,q}$ and $z_{0,t}$ that are one (medium blue) and two (light blue) orders of magnitude (OoM) smaller or larger, respectively, compared to the EC-derived roughness length values (see table S3).

Table S3. Roughness length values used for the sensitivity study shown in figure S6. The values for $z_{0,u}$, $z_{0,q}$ and $z_{0,t}$ are one and two orders of magnitude (OoM) smaller or larger, respectively, compared to the EC-derived roughness length values.

	$\pm$ 1 OoM	$\pm$ 2 OoM
$z_{0,u}$	$1.3\text{e}-5\,\text{m}$ to $1.3\text{e}-3\,\text{m}$	$1.3\text{e}-6\,\text{m}$ to $1.3\text{e}-2\,\text{m}$
$z_{0,q}$	$5.7\text{e}-8\,\text{m}$ to $5.7\text{e}-6\,\text{m}$	$5.7\text{e}-9\,\text{m}$ to $5.7\text{e}-5\,\text{m}$
$z_{0,t}$	$2.9\text{e}-5\,\text{m}$ to $2.9\text{e}-3\,\text{m}$	$2.9\text{e}-6\,\text{m}$ to $2.9\text{e}-2\,\text{m}$

S8 Bulk fluxes timeseries

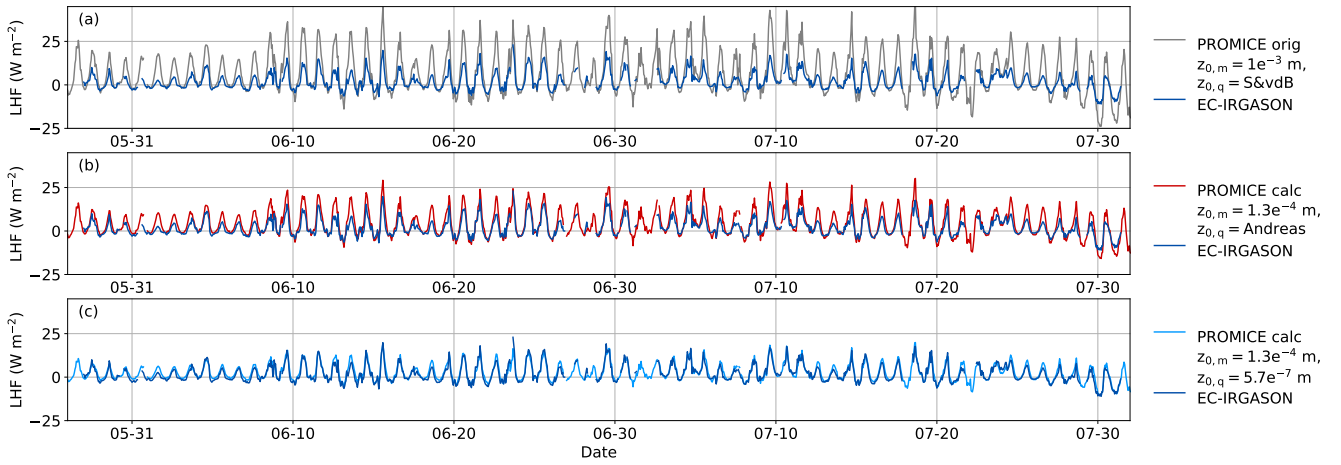

Figure S7. Timeseries of the bulk LHF based on the PROMICE AWS observations and EC-Irgason LHF. Panel (a) is based on the original PROMICE data product using $z_{0,m}$=1 $\times$ 10^{-3} m and $z_{0,q}$=$z_{0,t}$=(Smeets and Van den Broeke, 2008a, b)(S&vdB). Panel (b) is the bulk flux recalculated using the $z_{0,m}$ from the EC-Irgason and parameterizations from Andreas (1987). Panel (c) shows the calculated bulk flux using the $z_{0,m}$, $z_{0,q}$, and $z_{0,t}$ values derived from the EC-Irgason.

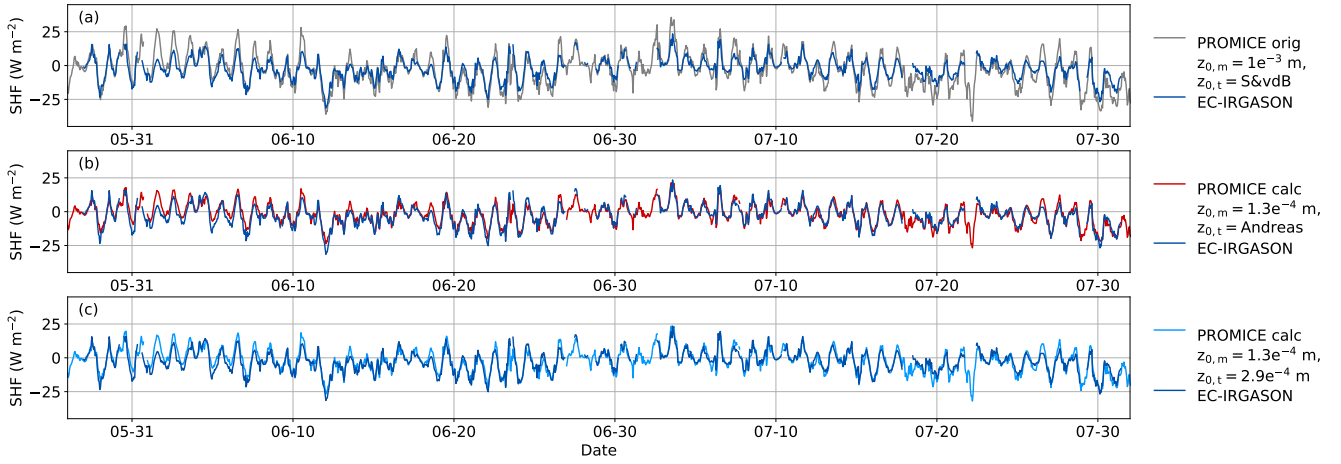

Figure S8. Timeseries of the bulk SHF based on the PROMICE AWS observations and EC-Irgason SHF. Panel (a) is based on the original PROMICE data product using $z_{0,m}$=1 $\times$ 10^{-3} m and $z_{0,q}$=$z_{0,t}$=(Smeets and Van den Broeke, 2008a, b)(S&vdB). Panel (b) is the bulk flux recalculated using the $z_{0,m}$ from the EC-Irgason and parameterizations from Andreas (1987). Panel (c) shows the calculated bulk flux using the $z_{0,m}$, $z_{0,q}$, and $z_{0,t}$ values derived from the EC-Irgason.

S9 Blowing Snow

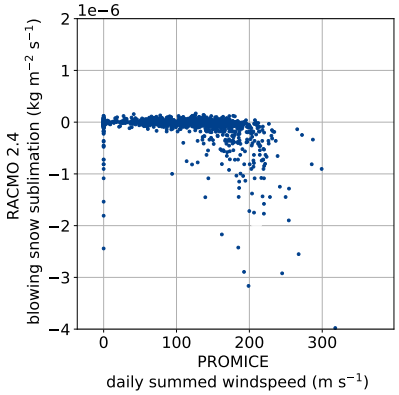

Figure S9. Scatter plot of the blowing snow sublimation in the lowest model layer at EastGRIP in RACMO2.4 (daily values) against the windspeed from the PROMICE AWS (daily sum of hourly values) from May 2016 until the end of 2019.

S10 PROMICE timeseries winter months

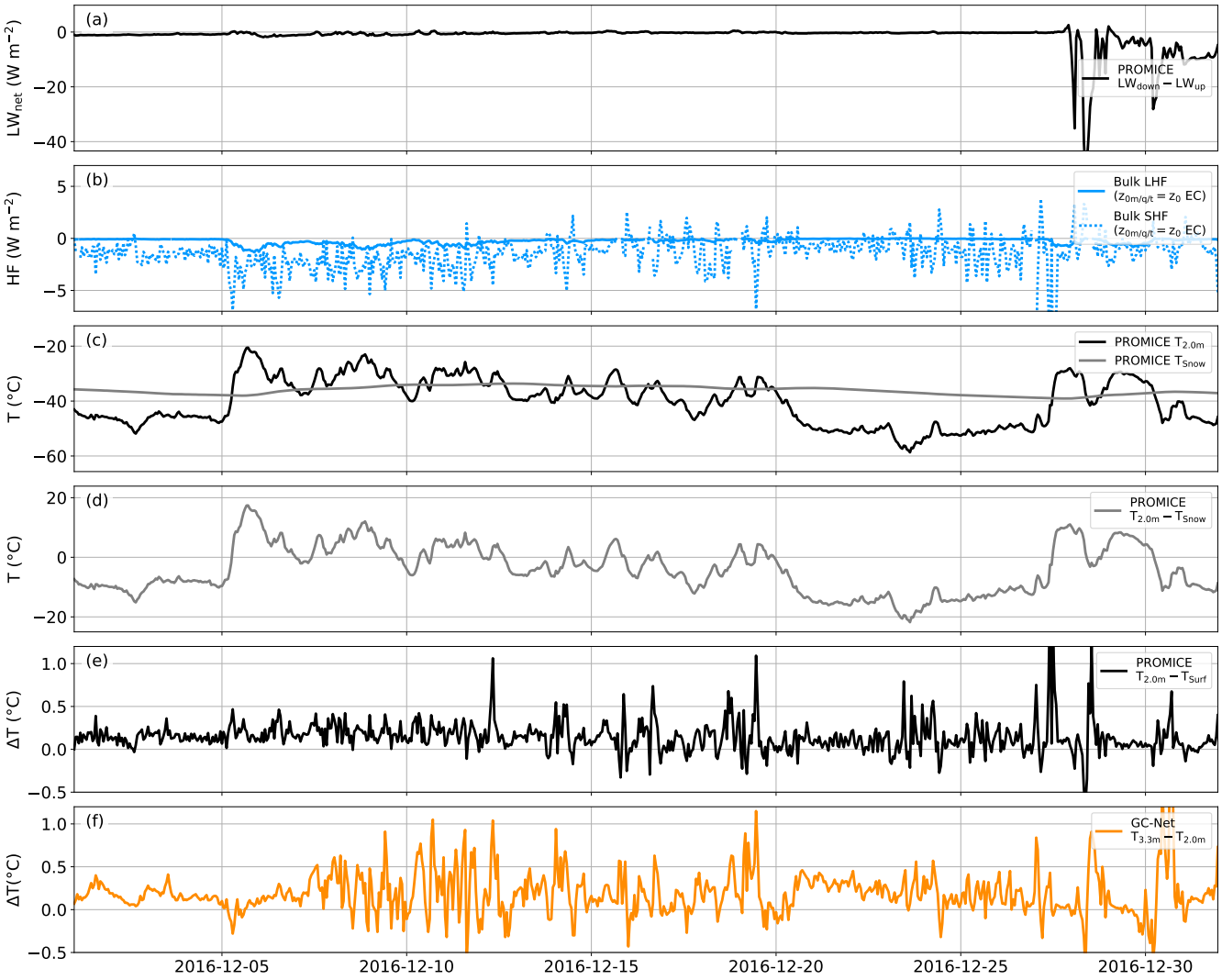

Figure S10. Time series of winter AWS observations in December 2016 with (a) the net longwave radiation, (b) the calculated sensible and latent heat flux, using the $z_{0,m}$, $z_{0,q}$ and $z_{0,t}$ values derived from the EC-Irgason, (c) the air temperature at 2.0 m above the surface and the snow temperature approximately 10 cm below the surface, (d) the temperature difference between the 2.0 m and snow temperature and (e) the PROMICE temperature difference between 2.0 m and the surface, determined via the longwave radiation and (f) the GC-Net temperature difference between 3.3 m and 2.0 m. Note that the complete dataset is shown for this figure, including the data below $-50\,^{\circ}$ C.

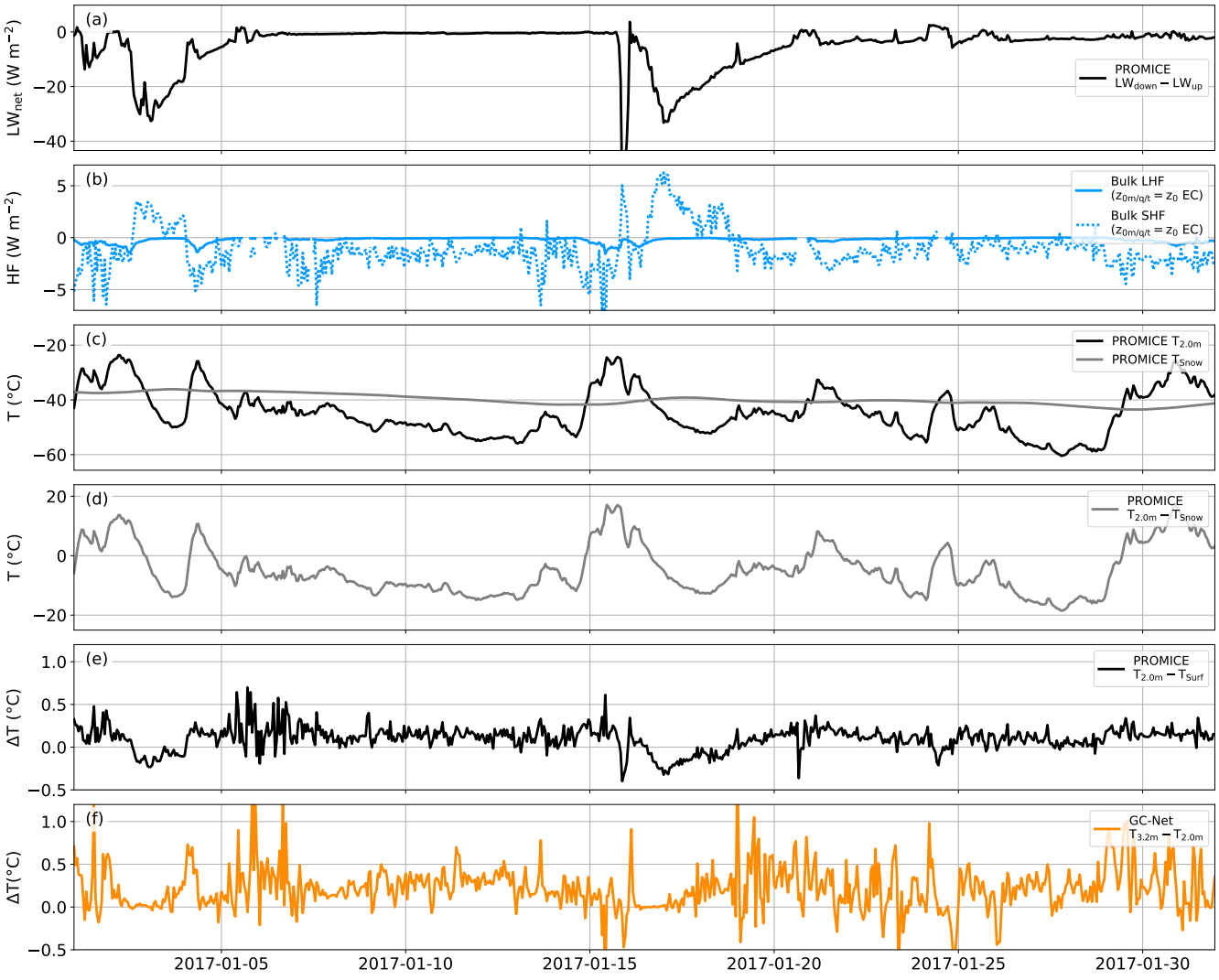

Figure S11. Time series of winter AWS observations in January 2017 with (a) the net longwave radiation, (b) the calculated sensible and latent heat flux, using the $z_{0,m}$, $z_{0,q}$ and $z_{0,t}$ values derived from the EC-Irgason, (c) the air temperature at 2.0 m above the surface and the snow temperature approximately 10 cm below the surface, (d) the temperature difference between the 2.0 m and snow temperature and (e) the PROMICE temperature difference between 2.0 m and the surface, determined via the longwave radiation and (f) the GC-Net temperature difference between 3.2 m and 2.0 m. Note that the complete dataset is shown for this figure, including the data below -50 ° C.

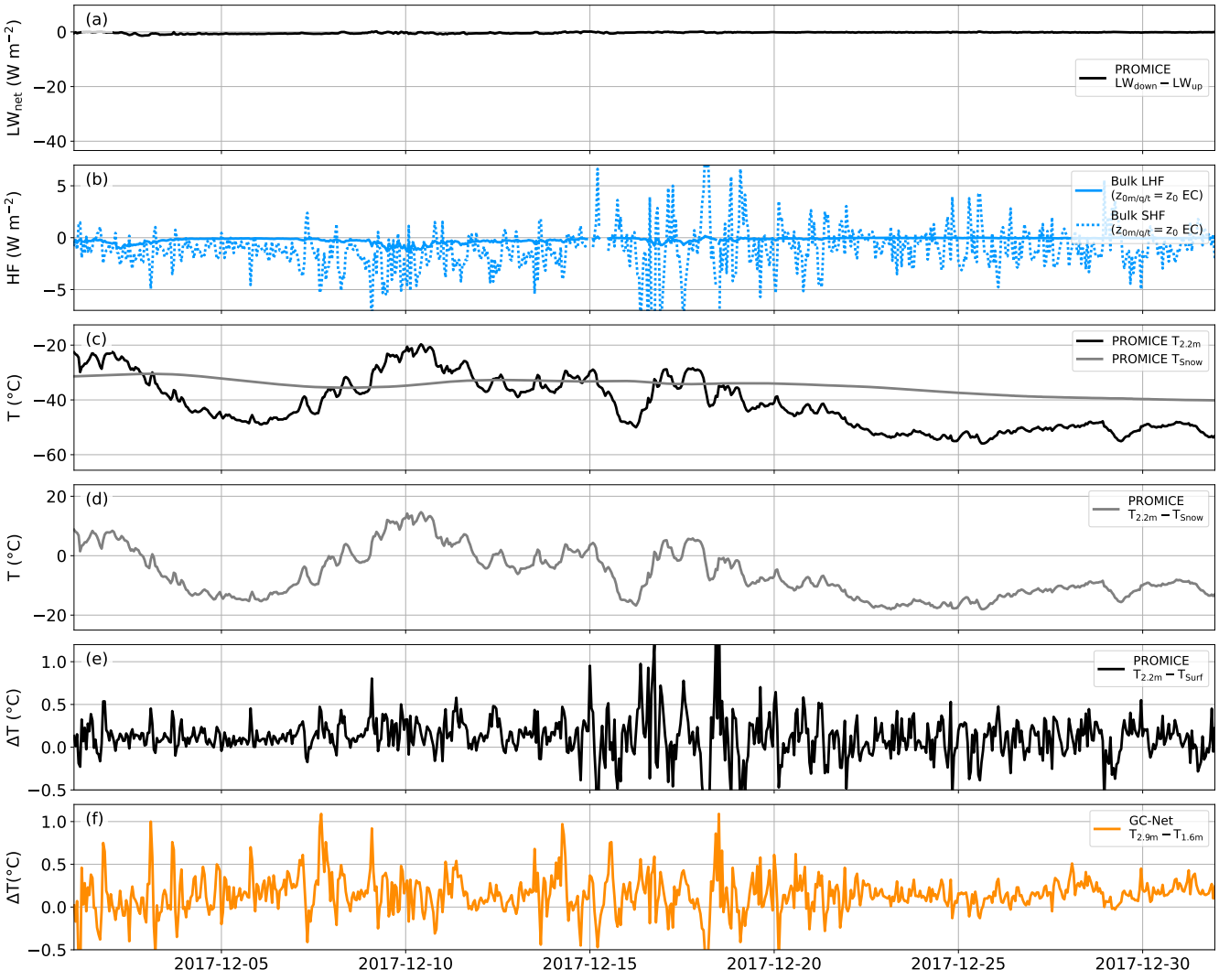

Figure S12. Time series of winter AWS observations in December 2017 with (a) the net longwave radiation, (b) the calculated sensible and latent heat flux, using the $z_{0,m}$, $z_{0,q}$ and $z_{0,t}$ values derived from the EC-Irgason, (c) the air temperature at 2.2 m above the surface and the snow temperature approximately 10 cm below the surface, (d) the temperature difference between the 2.2 m and snow temperature and (e) the PROMICE temperature difference between 2.2 m and the surface, determined via the longwave radiation and (f) the GC-Net temperature difference between 2.9 m and 1.6 m. Note that the complete dataset is shown for this figure, including the data below -50 ° C.

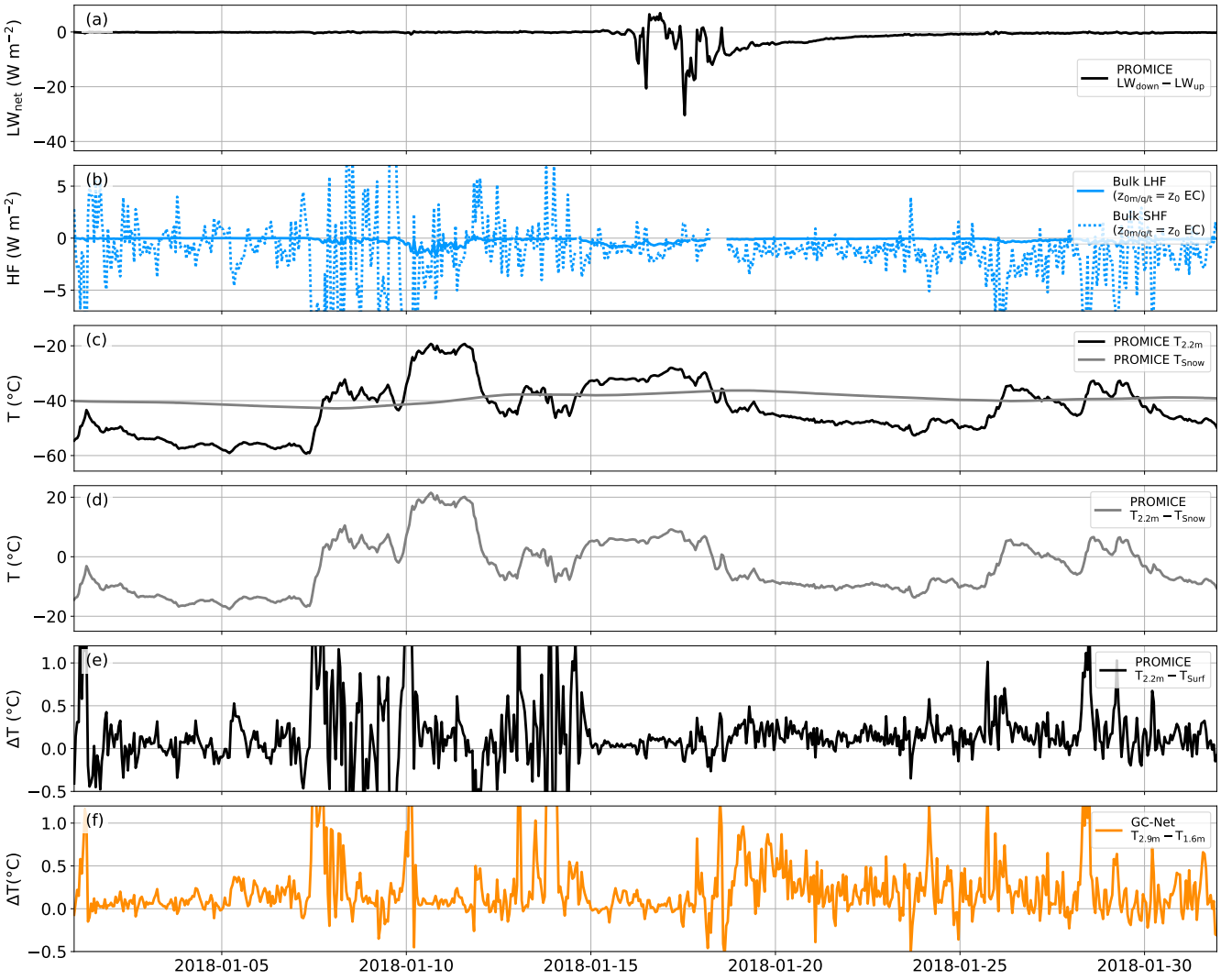

Figure S13. Time series of winter AWS observations in January 2018 with (a) the net longwave radiation, (b) the calculated sensible and latent heat flux, using the $z_{0,m}$, $z_{0,q}$ and $z_{0,t}$ values derived from the EC-Irgason, (c) the air temperature at 2.2 m above the surface and the snow temperature approximately 10 cm below the surface, (d) the temperature difference between the 2.2 m and snow temperature and (e) the PROMICE temperature difference between 2.2 m and the surface, determined via the longwave radiation and (f) the GC-Net temperature difference between 2.9 m and 1.6 m. Note that the complete dataset is shown for this figure, including the data below -50 ° C.

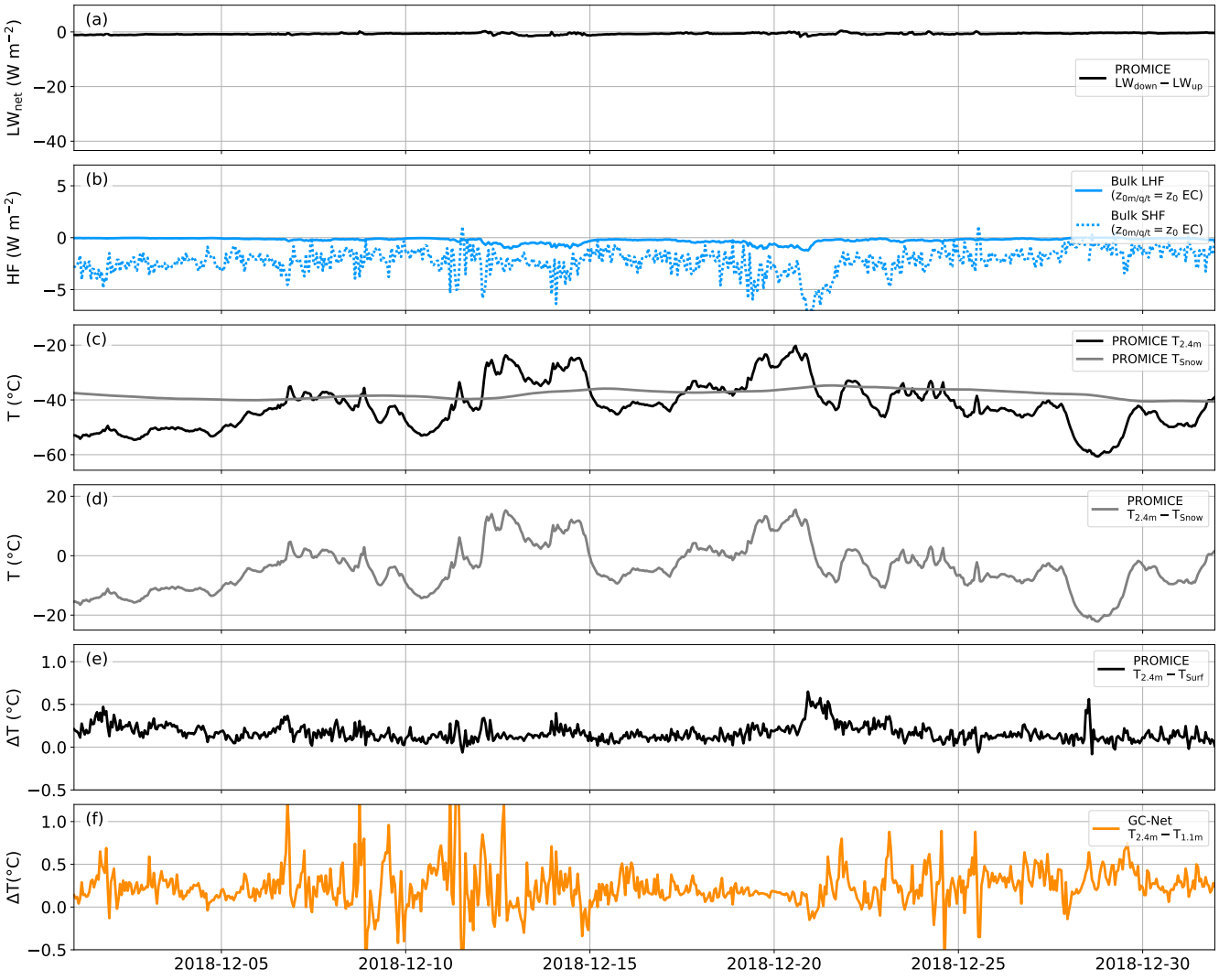

Figure S14. Time series of winter AWS observations in December 2018 with (a) the net longwave radiation, (b) the calculated sensible and latent heat flux, using the $z_{0,m}$, $z_{0,q}$ and $z_{0,t}$ values derived from the EC-Irgason, (c) the air temperature at $2.4\,\mathrm{m}$ above the surface and the snow temperature approximately $10\,\mathrm{cm}$ below the surface, (d) the temperature difference between the $2.4\,\mathrm{m}$ and snow temperature and (e) the PROMICE temperature difference between $2.4\,\mathrm{m}$ and the surface, determined via the longwave radiation and (f) the GC-Net temperature difference between $2.4\,\mathrm{m}$ and $1.1\,\mathrm{m}$. Note that the complete dataset is shown for this figure, including the data below $-50\,^\circ\,\mathrm{C}$.

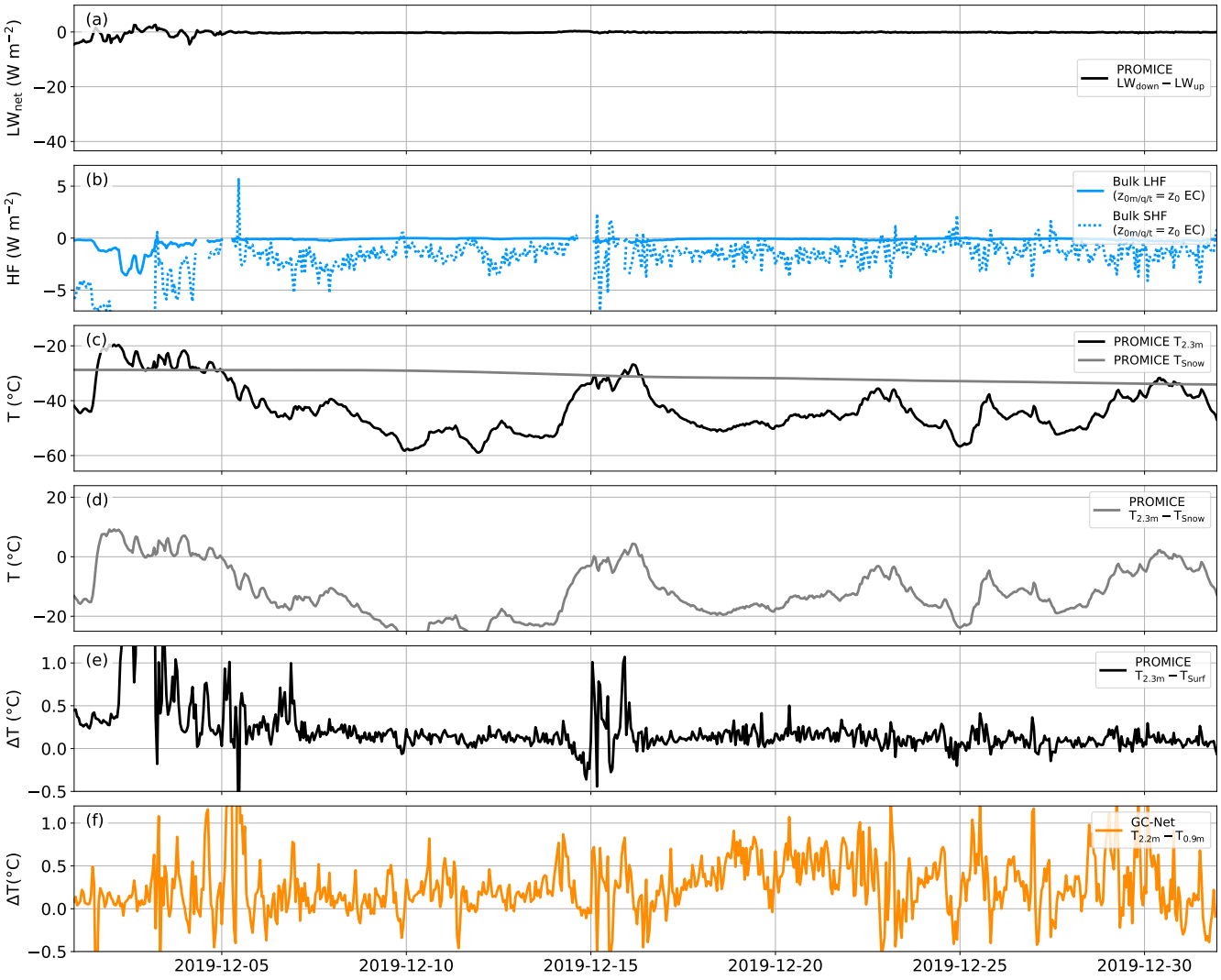

Figure S15. Time series of winter AWS observations in December 2019 with (a) the net longwave radiation, (b) the calculated sensible and latent heat flux, using the $z_{0,m}$, $z_{0,q}$ and $z_{0,t}$ values derived from the EC-Irgason, (c) the air temperature at 2.3 m above the surface and the snow temperature approximately 10 cm below the surface, (d) the temperature difference between the 2.3 m and snow temperature and (e) the PROMICE temperature difference between 2.3 m and the surface, determined via the longwave radiation and (f) the GC-Net temperature difference between 2.2 m and 0.9 m. Note that the complete dataset is shown for this figure, including the data below -50 ° C.

S11 PROMICE longwave radiation

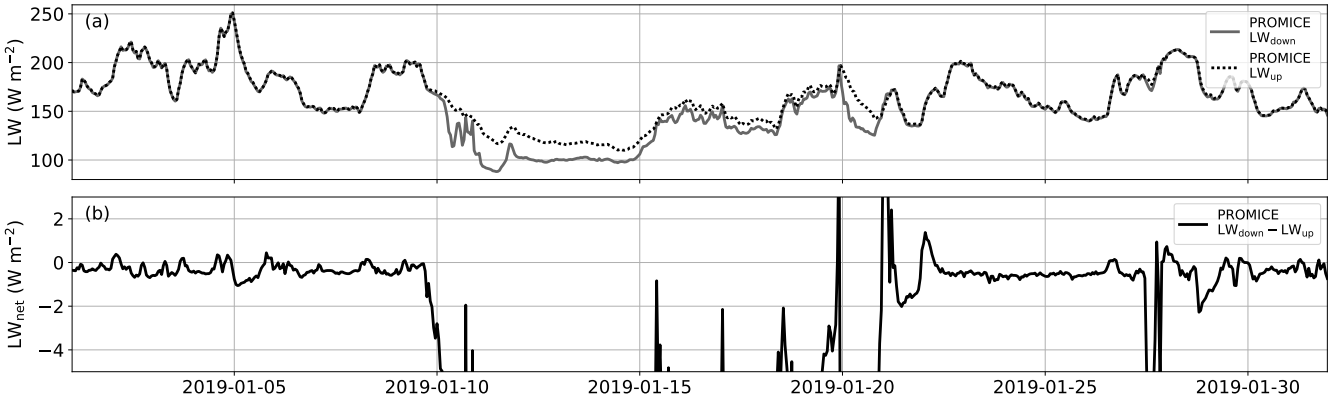

Figure S16. Time series of the PROMICE AWS winter longwave radiation observations with (a) the separate up- and downwards measured longwave radiation and (b) net longwave radiation on a magnified y-axis highlighting variability in the near-zero net radiation.

S12 Seasonal cycle temperature gradient and wind

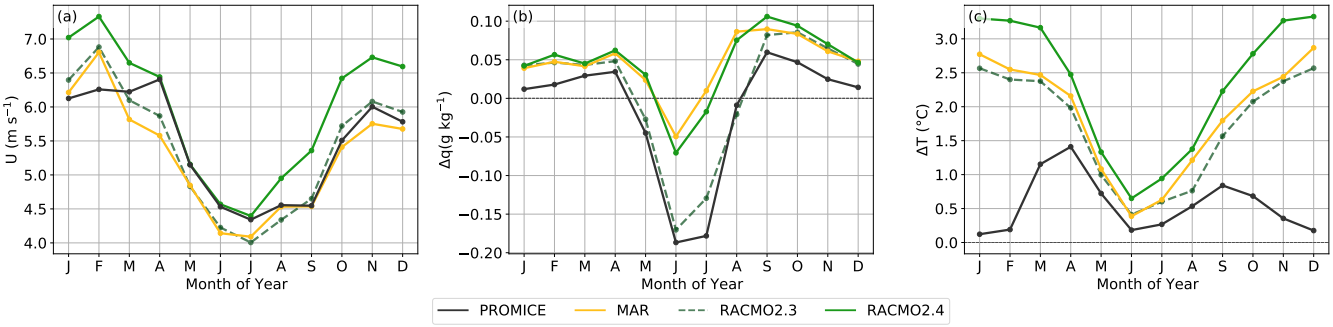

Figure S17. Seasonal cycle of the (a) windspeed, (b) specific humidity difference between 2 m and surface level and (c) temperature difference between 2 m and surface level from the PROMICE AWS and RCM's MAR, RACMO2.3 and RACMO2.4 from May 2016 until the end of 2019.

References

Andreas, E. L.: A theory for the scalar roughness and the scalar transfer coefficients over snow and sea ice, Boundary-Layer Meteorology, 38, 159–184, https://doi.org/10.1007/BF00121562, 1987.

Kaimal, J. C., Wyngaard, J. C., Izumi, Y., and Coté, O. R.: Spectral characteristics of surface-layer turbulence, Quarterly Journal of the Royal Meteorological Society, 98, 563–589, https://doi.org/https://doi.org/10.1002/qj.49709841707, 1972.

Kljun, N., Calanca, P., Rotach, M. W., and Schmid, H. P.: A simple two-dimensional parameterisation for Flux Footprint Prediction (FFP), Geoscientific Model Development, 8, 3695–3713, https://doi.org/10.5194/gmd-8-3695-2015, 2015.

Mauder, M. and Foken, T.: Eddy-Covariance Software TK3, https://doi.org/10.5281/zenodo.611345, type: software, 2015.

Moore, C. J.: Frequency response corrections for eddy correlation systems, Boundary-Layer Meteorology, 37, 17–35, https://doi.org/10.1007/BF00122754, 1986.

Rozmiarek, K. S., Dietrich, L. J., Vaughn, B. H., Town, M. S., Markle, B. R., Morris, V., Steen-Larsen, H. C., Fettweis, X., Brashear, C. A., Bennett, H., and Jones, T. R.: Atmosphere to Surface Profiles of Water-Vapor Isotopes and Meteorological Conditions Over the Northeast Greenland Ice Sheet, Journal of Geophysical Research: Atmospheres, 130, e2024JD042 719, https://doi.org/https://doi.org/10.1029/2024JD042719, e2024JD042719 2024JD042719, 2025.

Smeets, C. J. P. P. and Van den Broeke, M. R.: The Parameterisation of Scalar Transfer over Rough Ice, Boundary-Layer Meteorology, 128, 339–355, https://doi.org/10.1007/s10546-008-9292-z, 2008a.

Smeets, C. J. P. P. and Van den Broeke, M. R.: Temporal and Spatial Variations of the Aerodynamic Roughness Length in the Ablation Zone of the Greenland Ice Sheet, Boundary-Layer Meteorology, 128, 315–338, https://doi.org/10.1007/s10546-008-9291-0, 2008b.

Van Tiggelen, M.: Roughish ice, snow and turbulent heat fluxes on the Greenland ice sheet, https://doi.org/10.33540/1703, 2023.